Upgrading syngas from wood gasification through steam reforming of tars over highly active Ni-perovskite catalysts at relatively low temperature

Lole Jurado, Vasiliki Papaefthimiou, Sébastien Thomas, Annecécile Roger

Upgrading syngas from wood gasification through steam reforming of tars over highly active Ni-perovskite catalysts at relatively low temperature

Lole Jurado[¥]*, *Vasiliki Papaefthimiou, Sébastien Thomas, Anne-Cécile Roger*

Institute of Chemistry and Processes for Energy, Environment and Health, ECPM, UMR 7515, University of Strasbourg, 25 rue Becquerel, F-67087 Strasbourg, France

[¥]Current affiliation : Laboratoire de Chimie de Coordination, UPR CNRS 8241, Université de Toulouse, 205 Route de Narbonne, 31077 Toulouse Cedex 4 France.

***Corresponding author:** Lole Jurado (dolores.juradofuentes@lcc-toulouse.fr)

Abstract.

Tar formation during biomass gasification causes several operational problems, besides limiting the downstream application of the syngas produced. The development of an efficient catalyst for tar reforming at mild temperature is targeted. In this study, La-based perovskite ($La_{0.6}Sr_{0.4}Co_{0.2}Fe_{0.8}O_{3-\delta}$)-supported Ni materials have been synthesized through wetness impregnation (Ni/LSCF) and one-pot sol-gel method (Ni-LSCF). As-prepared catalysts have been characterized by N_2 physisorption, XRD, TPR, H_2-TPD and XPS. The impact of the synthesis path and the effect of Ru have been evaluated in steam reforming of toluene and phenol at low temperature (550 ºC) under a model syngas. Regardless the tar model molecule, similar catalytic stability and activity toward tar reforming were attained for both Ni/LSCF and Ni-LSCF. However, a better catalytic performance toward WGS and higher resistance to coke formation was evidenced for Ni-LSCF than for Ni/LSCF. This better behavior has been mainly ascribed to the high Sr content at its surface, pointing out the key role of the basic elements at the catalytic surface in the activity and stability in steam reforming of tars. The addition of Ru led to

an enhancement in the catalytic activity for toluene reforming, while no noticeable improvement was attained for phenol reforming.

Keywords: Tar reforming, perovskites, Ni catalysts, Ruthenium, biomass gasification

1. Introduction

Biomass gasification is a potential biomass conversion technology for the production of energy or of valuable gas, known as syngas, used in the synthesis of biofuels or chemical products, such as methanol [1,2]. Nevertheless, the tar formation as undesired by-products is one of the main drawbacks of this approach. Tar is a sticky and dark complex mixture of light and aromatic heavy hydrocarbons, with toluene as the major component [3]. The condensation of this mixture at ambient or moderate temperature can bring wide range of operational and environmental problems, counting the plugging and the fouling of turbines, pipelines and engines as well as the water pollution [1,4,5]. Moreover, the presence of tars in the product syngas could limit its use in some further downstream applications [6]. Conventional thermochemical process for tar removal, such as thermal cracking, requires high temperatures and/or an increment of the gas residence time, generating a large amount of soot [7]. The overall efficiency of the process can be improved by using a catalytic system. To date, steam reforming of tars has taken particular attention, since tar can be easily converted into H_2, CH_4 and CO at much lower temperature than that use in non-catalytic process. Afterwards, the product CO might simultaneously react with the steam through water gas shift (WGS) reaction to form H_2-rich syngas, upgrading the quality of the raw syngas [8–10]. Supported-Ni catalysts have been widely used in the industry for steam reforming reaction of tar due to its acceptable activity and low cost [11]. However, these catalysts can undergo catalytic deactivation through metal sintering and/or coke deposits when they are submitted to the harsh environment generated under biomass gasification conditions [12,13]. Accordingly,

many studies have been focused on the modification of the catalytic support in order to enhance the catalytic activity and stability by improving the metal dispersion and inhibiting the coke deposits. Supports with high oxygen mobility and oxygen storage capacity play a crucial role in the catalytic activity and stability in reforming reactions. The presence of high concentration of oxygen vacancies and mobile oxygen species in or on the support can facilitate the water activation during steam reforming reactions, boosting the gasification of coke deposits through oxygen supply to the active phase.

Perovskite-based materials (ABO_3) could be a promising catalytic support in steam reforming reaction due to their high lattice oxygen mobility [14]. In the general formula, the A-site is usually occupied by lanthanide, alkaline or alkaline earth cation whereas the B-site is composed by any transition metal cation as Mn, Co, Fe, Ni. The substitution of the A and/or B sites with other aliovalent ions and/or with different cationic radius have been studied for those kinds of materials. The distortion in the crystalline structure due to the addition of these ions causes structural defects in the perovskite lattice, leading to the formation of oxygen vacancies and, thus, to a high content of mobile oxygen species [14–16]. Among the infinite possible composition of a perovskite oxide, the lanthanum-containing perovskites have been widely investigated and have shown an outstanding catalytic performance in steam reforming of tar. Thereby, the partial insertion of alkaline earth elements (Ca^{2+}, Sr^{2+}) substituting La^{3+} into the A-sites induces nonstoichiometric oxygen into the perovskite structure [17]. Owing to its atomic size, strontium (Sr) has been extendedly used as a dopant on the A-site, introducing oxygen vacancies in the perovskite structure [14,18]. For instance, Oemar *et al*. [15] found that Ni/$La_{0.8}Sr_{0.2}AlO_3$ shown the best catalytic activity and resistance to coke in steam reforming of toluene, among Ni/$LaAlO_3$, Ni/$La_{0.8}Sr_{0.2}AlO_3$, Ni/La_2O_3 and Ni/α-Al_2O_3. The authors associated the high catalytic performance to an increase in the content of the oxygen vacancies over

the catalytic surface for $Ni/La_{0.8}Sr_{0.2}AlO_3$ due to the lattice distortion caused by Sr doping. Besides, the effect of Mg, Ca and Sr doping into the $LaNi_{0.8}Fe_{0.2}O_3$ (LNFO) perovskite in steam reforming of toluene has been investigated [19]. The higher number of active sites and lattice oxygen species displayed for the Sr-doped LNFO catalyst gives rise to an improvement in the catalytic activity and in the resistance to coke deposits. Sekine *et al.* [20] observed by transient isotopic tests that the substitution of La by Sr cations into the $La_{0.7}Sr_{0.3}AlO_3$ perovskite structure could activate the lattice oxygen species to enhance toluene reforming and suppress the carbon formation. Furthermore, the use of cations of high valence into the B-site (Fe, Co or Cr) provides redox active sites that determine the adsorption/desorption of hydroxyl groups and may facilitate the steam activation during steam reforming reaction [14,21].

In the present work, Ni-based catalysts using a Sr-doped lanthanum-based perovskite, of composition $La_{0.6}Sr_{0.4}Co_{0.2}Fe_{0.8}O_{3-\delta}$, as catalytic support has been prepared through traditional wetness impregnation and one-spot sol-gel method. The impact of the synthesis path as well as the effect of Ru as dopant have been evaluated in steam reforming reaction of tar. Up to now, most of the studies focused on the steam reforming of tar carried out at laboratory scale have been performed using a mixture of a model tar molecule and water for a better understanding of the reaction mechanism. Nevertheless, the conditions at industrial scale are largely different (syngas composition, presence of particles, sulphur compounds, ashes, …). Accordingly, steam reforming of toluene and phenol under model syngas composition have been investigated at relatively low temperature (550 ºC) in order to simulate industrial conditions. As the final goal would be the use of these materials in a downstream reactor at the outlet of a gasifier at pilot plant scale, the catalytic reaction conditions employed in this study have been mainly

built upon the composition and the temperature of the syngas produced from the wood gasification at large scale.

2. Experimental

2.1. Support and catalysts synthesis

Perovskite type oxide, $La_{0.6}Sr_{0.4}Co_{0.2}Fe_{0.8}O_{3-\delta}$ (LSCF), was prepared by pseudo sol-gel synthesis route. It is based on thermal decomposition of the associated mixed propionate precursor as it has been described in prior work [3]. The associated lanthanum (III), strontium (II), cobalt (II) and iron (II) metal acetates were used as starting salts. The resulting mixed propionate precursor was dried under air at 100 ºC and then, it was calcined at 800 ºC for 6 h with a heating ramp of 2 $ºC \cdot min^{-1}$.

The addition of 10 wt% metallic nickel has been performed by two different pathways: (1) via *pseudo sol-gel route during perovskite synthesis* (Ni-LSCF) and (2) via *wetness impregnation* of the LSCF support oxide (Ni/LSCF). In the former, nickel (II) acetate was used as starting salt and it was introduced instantaneously in the pseudo sol-gel synthesis during the support preparation. In the latter, nickel (II) nitrate tetrahydrate solved in few millilitres of ethanol was added over the support. The mixture was stirred during 20 min and dried in air at 100 ºC until complete evaporation of the ethanol. Lastly, the impregnated mixed oxide was calcined under air at 500 ºC for 6 h using a ramp of 5 $ºC \cdot min^{-1}$. Additionally, a loading of 1 wt% of metallic Ru was added over the Ni/LSCF catalyst by a second wetness impregnation, resulting in RuNi/LSCF catalyst. Same impregnation procedure as for the Ni/LSCF catalyst was followed, using ruthenium (III) acetylacetonate as starting salt.

2.2. Characterization techniques

The elemental composition of the materials was measured by X-ray fluorescence spectrometry (XRF) on a PANalytical AXIOS PW440 sequential spectrophotometer equipped with a rhodium tube as source of radiation.

The specific surface area (SSA) and pore volume (V_{pore}) were determined through N_2 physisorption at 77 K on a Micrometrics sorptometer Tri Star 3000. The samples were previously outgassed at 250 ºC for 3 h in order to remove the moisture adsorbed at the surface and inside the pores.

The crystalline phases of the fresh and spent materials were evaluated by X-ray diffraction (XRD) on a Bruker D8 Advance diffractometer with LynxEye detector side and Ni filtered Cu K_α radiation (1.5418 Å). The diffractograms were collected between 20 and 85º with a step size of 0.05º and step time of 1.6 s. The crystallite sizes of the support ($d_{support}$) and NiO (d_{NiO}) have been calculated for the fresh materials using the well-known Debye-Scherrer equation. Reticular planes (112) and (204) placed at $2\theta \sim 33$ and 58º were used for the support, while reticular planes (111) and (200) at $2\theta \sim 37$ and 43º were considered for the NiO phase. Besides, the pseudo cubic lattice parameter (a) of the support has been averaged out.

The reducibility and the metal-support interaction as well as the metallic surface were evaluated by temperature programmed reduction (H_2-TPR) and H_2-temperature programmed desorption (H_2-TPD), respectively. Both techniques were conducted on a Micromeritics AutoChem II fitted with a thermal conductivity detector (TCD). For H_2-TPR analysis, an amount of around 50 mg of fresh samples was heated up to 950 ºC using a heating ramp of 15 ºC min^{-1} under a 10 mol% H_2/Ar atmosphere (50 NmL min^{-1}). The TPR profiles normalized with respect to the mass of the sample as a function of the temperature are shown. The support reducibility was determined from the H_2 consumption, assuming the complete NiO reduction to Ni^0 and B-cation sites (Co^{3+} and

Fe^{3+}) as the only reducible species in the perovskite oxide. For H_2-TPD analysis, around 100 mg of fresh samples were pre-reduced simulating pretreatment conditions performed before the catalytic reaction. Thereby, samples were reduced in a 10 mol% H_2/Ar at 600 ºC for 2 h with a ramp of 2 ºC·min^{-1}. Afterwards, the reduced samples were exposed to Ar gas flow for 90 min, following by the injection of 15 pulses of 10 %mol H_2/Ar with a loop of 50 μL at atmospheric pressure and 50 °C. Lastly, TPD was conducted by heating the samples upon 950 ºC under Ar atmosphere using a ramp of 10 ºC·min^{-1}. Similarly, the TPD profiles normalized with respect to the mass of the sample as a function of the temperature are presented. Additionally, the metallic surface was calculated by considering only the exposed surface per atom of Ni (6.51 $Å^2$) [22] since this metal is prevailing in the catalysts compared to the others (Co, Fe or Ru). This calculation has been detailed in a previous work [3].

The chemical surface composition and the oxidation state of the different elements at the surface of the fresh materials were evaluated by X-ray photoelectron spectroscopy (XPS). The XP spectra were recorded on an ultrahigh vacuum spectrometer fitted with a RESOLVE 120 MCD5 hemispherical electron analyzer using Al Kα (hv=1486.6 eV) as incident radiation. Both, survey, and high-resolution spectra, were acquired using a constant pass energy mode of 100 and 20 eV, respectively. The C(1s) peak, placed at 284.6 eV, was employed as reference for rectifying the binding energy values from possible charge effects. The area of the core level peaks was used for estimating the atomic surface content of the different elements.

The carbon deposits generated over the catalytic surface during tar reforming reaction was characterized by thermogravimetric analysis (TGA) of the spent catalysts on a Q 5000IR from TA instrument. A quantity of 3 mg of spent catalyst was heated up to 900 ºC under air gas flow of 25 NmL·min^{-1} using a ramp of 10 ºC·min^{-1}. Additionally, the

spent catalysts were analyzed by scanning electron microscopy (SEM) on a Zeiss GeminiSEM 500 microscope with an electron source based on FEG Schottky for determining the morphology of these carbon deposits.

2.3.Catalytic tests

The catalytic tests have been performed under isothermal conditions at 550 ºC for 6 h at atmospheric pressure in a fixed-bed quartz reactor using a fresh catalytic bed for each reaction. Prior to the catalytic tests, the catalytic systems were reduced *in situ* using a mixture of 40 mol% H_2/N_2 with a total gas flow of 77 NmL min^{-1} at 600 ºC for 2 h using a heating ramp of 2 ºC min^{-1}. A scheme of the experimental set-up for each tar model molecule has been reported in our previous work [3]

Toluene and phenol were used as tar model molecule. The molecules were fed one-by-one along with a simulated molar gas composition (2% CH_4, 10% H_2O, 12% CO_2, 16% H_2 and 20% CO, balanced with N_2). A total gas flow rate and a catalytic loading of 139 NmL min^{-1} and 23 mg was respectively used ($WHVS_{gas}$, 370 h^{-1}). For toluene reforming, an inlet molar toluene content of 0.19% was fed into the reactor through a saturator at -20 ºC using a mixture of CO_2 and N_2 with a total gas flow of 73 NmL·min^{-1}. The steam-carbon molar ratio, S/C_{tar}, determined by assuming only the moles of carbon in the tar molecule, was 7.7 and the tar weight hourly space velocity ($WHSV_{tar}$, *Equation 1*) was 2.6 h^{-1}. For phenol reforming, an inlet molar phenol content of 0.10% was fed into the reactor by pumping a liquid flow of 10.4 μL min^{-1} of an aqueous phenol solution with a composition of 1.0 mol%. In this case, the reaction was carried out operating with slightly lower $WHSV_{tar}$ (1.4 h^{-1}) and lower the S/C_{tar} ratio (16.5) than for toluene reforming. These reaction conditions have been selected based on the real syngas composition produced from a biomass gasification process at pilot plant scale as it has been already reported in prior work [3].

$$\mathrm{WHSV_{tar}(h^{-1})} = \frac{\text{Total tar mass flow } (g \cdot h^{-1})}{\text{Mass of catalyst (g)}} \qquad (\textit{Equation 1})$$

The variation of the gaseous feed flows at the outlet of the catalytic reactor were analyzed online by gas chromatography. The condensable products were recovered with two traps in toluene reforming, whereas one trap was used in phenol reforming. In toluene reforming, the first trap was in water-ice bath (0 ºC) to mostly collect the outlet water, whereas the second one was placed in an acetone-dry ice bath (-77 ºC) to condense the non-converted toluene and other derivatives. One trap placed in water-ice bath (0 ºC) was used for phenol reforming. Lastly, the recovered liquid phases have been weighed and analyzed by off-line gas chromatography fitted with a flame ionization detector (FID).

The average tar conversion (X_{tar}), the selectivity to benzene for toluene reforming ($S_{benzene}$) and the selectivity to carbon deposits (S_{coke}) estimated from TGA analysis were defined as follow:

$$X_{tar} = \frac{n_{C\ tar,in} - n_{C\ tar,out}}{n_{C\ tar,in}} \qquad (\textit{Equation 2})$$

$$S_{benzene} = \frac{n_{C,benzene}}{n_{converted\ C}} \qquad (\textit{Equation 3})$$

$$S_{coke}(\%) = \frac{total\ mol\ deposited\ coke}{n_{C\ tar,in} \cdot X_{tar}} \qquad (\textit{Equation 4})$$

Additionally, the outlet molar flow rate of the gaseous compounds (H_2, CO, CO_2 and CH_4) versus the time on stream for each catalytic test was also presented.

3. Results and discussion

3.1. Characterization of the fresh support and catalysts

The nominal bulk composition and the one determined by XRF analysis are shown in ***Table 1*** for the as prepared materials. By comparing with the nominal composition, a lower amount of La and Fe is achieved for all the materials, while the amount of Sr and

Co incorporated was higher. Regardless the synthesis path, similar bulk composition is attained for the metal-containing catalysts, being approximately: 20 at% La, 20 at% Sr, 11 at% Co and 30 at% Fe. Concerning the metal content, the Ni content, varied between 20.7 at% and 21.6 at%, was also alike among the three catalysts and always higher than the expected value (17.3 at%), whereas the Ru content was the targeted one (1 at%). The differences between both, actual and nominal compositions, may arise from an unstable hydration state of the starting salts.

Table 1. *Bulk cationic composition obtained by XRF and nominal composition (in parenthesis) for the prepared materials*

	La (at%)	***Sr (at%)***	***Co (at%)***	***Fe (at%)***	***Ni (at%)***	***Ru (at%)***
LSCF	26.2 (30.0)	24.6 (20.0)	12.2 (10.0)	37.0 (40.0)	-	-
Ni/LSCF	19.5 (25.0)	20.9 (16.5)	9.7 (8.3)	29.2 (33.0)	20.7 (17.3)	-
Ni-LSCF	19.1 (25.0)	18.8 (16.5)	11.0 (8.3)	29.6 (33.0)	21.6 (17.3)	-
RuNi/LSCF	16.5 (24.5)	20.7 (16.3)	11.3 (8.2)	29.5 (32.7)	21.0 (17.3)	1.1 (1.0)

A summary of the physicochemical properties of the prepared materials is reported in ***Table 2.*** A low SSA was found for all the materials, ranged from 7 to 14 $m^2 \cdot g^{-1}$. These low values are caused by the high calcination temperature required to form their crystalline structure and are characteristic of the perovskite type oxides synthesized through sol-gel method [14,23]. Regardless the method, the addition of Ni leads to an increase of the SSA for both Ni containing LSCF systems (14 $m^2 \cdot g^{-1}$ for Ni/LSCF and 10 $m^2 \cdot g^{-1}$ Ni-LSCF) with respect to the bare LSCF oxide (7 $m^2 \cdot g^{-1}$), reaching the highest SSA through wetness impregnation. As expected, a low V_{pore} are shown for all the materials, ranged from 0.03 to 0.08 $cm^3 \cdot g^{-1}$, typical of non-porous solids. No huge modification in the textural properties by the impregnation of Ru over Ni/LSCF (RuNi/LSCF), compared to its bare Ni/LSCF catalyst, are evidenced.

Table 2. *Physicochemical properties of the prepared materials*

	SSA[a] ($m^2 \cdot g^{-1}$)	V_{pore}[a] ($cm^3 \cdot g^{-1}$)	$d_{support}$[b] (nm)	d_{NiO}[b] (nm)	$a_{support}$[b] (Å)	Support reducibility[c] (%)	$S_{metallic}$[d] ($m^2 \cdot g^{-1}$)
LSCF	7	0.04	15	-	3.872	29	-
Ni/LSCF	14	0.06	17	-	3.871	54	1.9
Ni-LSCF	10	0.03	14	26	3.865	72	0.5
RuNi/LSCF	13	0.08	14	-	3.876	56	2.1

[a]***from N_2 physisorption***
[b]***calculated from XRD analysis***
[c]***calculated from H_2 consumption (H_2-TPR)***
[d]***calculated from desorbed H_2 (H_2-TPD)***

The diffractograms of the fresh support and the catalytic systems are shown in ***Fig 1***. Two crystalline phases with different relative intensities are appreciated for the bare LSCF oxide. The predominant crystalline structure is related to a perovskite structure with orthorhombic symmetry ($La_{0.7}Sr_{0.3}Fe_{0.7}Co_{0.3}O_3$, JPCD 01-089-1268). The secondary phase corresponds to the formation of lanthanum oxide (La_2O_3, JPCD 01-083-1344). It reveals that the insertion of La^{3+} ions into the perovskite structure is not complete. No evidence of other crystalline phases related to Sr-, Co- or Fe- single or to mixed oxide structures are shown for the bare LSCF support. The crystallization of La_2O_3 as the only single oxide can be due to an excess of La added or to an excess of Sr incorporated in the A-site of the perovskite structure, rejecting part of La from the structure. According to the results reported in ***Table 1,*** the formation of La_2O_3 as secondary crystalline phase can be due to the excess of Sr detected for the bare LSCF by XRF analysis. The perovskite structure remained stable in both Ni/RuNi containing catalysts ((Ru)Ni/LSCF and Ni-LSCF) however, La_2O_3 phase does no longer appear, despite that the excess of Sr was found for these catalysts as well (***Table 1***). The peak position linked to the reticular plane (112) of the perovskite structure (***inset Fig 1***) exhibits a slight shift to higher 2θ for the sol-gel catalyst (Ni-LSCF) compared to the support (LSCF) and the equivalent catalyst (Ni/LSCF). This displacement points out that a partial insertion of $Ni^{2+/3+}$ ions into the

perovskite structure through sol-gel method might be favored, generating its cell contraction. For steric reasons, this partial insertion of Ni is highly favored as Ni^{3+} ions in the B-site cations of the perovskite [24]. Besides, an additional crystalline phase associated to NiO (JPCD 03-065-2901) is clearly observed for the sol-gel catalyst (Ni-LSCF) and no visible for the two impregnated ones ((Ru)Ni/LSCF). The absence of both, NiO and La_2O_3 phases, for the (Ru)Ni/LSCF catalysts indicates that a secondary perovskite ($LaNiO_3$) may be generated by the impregnated Ni and the excess of La_2O_3 observed in the diffractogram of the bare LSCF. This phase cannot be observable due to the overlap between the diffraction peaks of the $LaNiO_3$ phase, related to a hexagonal phase, and those associated to the LSCF one. In addition to the likely formation of $LaNiO_3$, the presence of well crystallized NiO particles of around 5 nm has been evidenced by TEM (see supplementary materials) for the impregnated materials ((Ru)Ni/LSCF). The absence of La_2O_3 phase for the sol-gel catalyst (Ni-LSCF) suggests that the introduction of La into the perovskite structure is facilitated by the partial insertion of the Ni ions. Due to the low content (and probably the small crystallites) of Ru added, the RuO_2 phase is not detected in the diffractogram of the RuNi/LSCF catalyst.

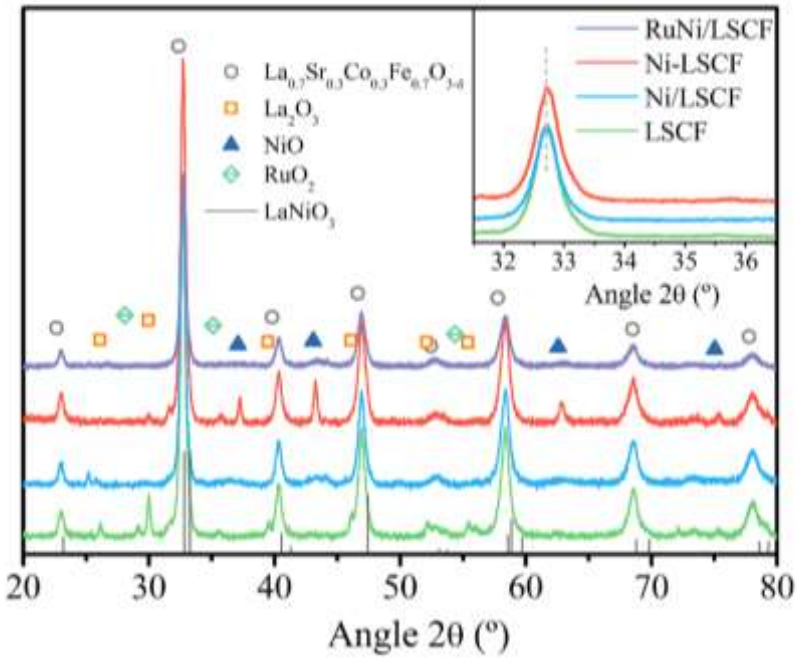

Fig 1. *Diffractograms of the prepared materials*

The support and the NiO crystallite size ($d_{support/NiO}$) as well as the pseudo cubic lattice parameter ($a_{support}$) of the prepared materials are listed in ***Table 1.*** Regardless the synthesis method, similar support crystallite size ($d_{support}$) was found for all the materials, around 14-17 nm. The relatively high NiO crystallite size reached for the sol-gel catalyst (26 nm) could be associated to a possible sintering process of the rejected NiO caused by the high calcination temperature used for its preparation (800 ºC). The pseudo cubic lattice parameter related to an elemental perovskite into a cubic system was determined by the cube root of the normalized perovskite cell volumes, V/z; being $V = a \times b \times c$ and $z = 4$ for the orthorhombic systems. In order to estimate the cell volume, the reticular parameters a, b and c were calculated using the diffraction peaks at 32.7º, 40.3º and 58.4º associated respectively to the (112), (022) and (204) reticular planes. The partial Ni insertion is clearly proved by comparison of the pseudo cubic lattice parameter of the impregnated catalysts and the sol-gel one. Indeed, the (Ru)Ni impregnation has not significant effect on the support lattice parameter (3.871 Å for Ni/LSCF and 3.876 Å for RuNi/LSCF) compared to the bare LSCF (3.872 Å), whereas a much lower value is shown

for the sol-gel catalyst, Ni-LSCF (3.865 Å). Therefore, as prior observed by XRD, the existence of Ni partially inserted into the LSCF oxide structure leads to a shift to higher 2θ for Ni-LSCF catalyst (***inset Fig 1***), since the ionic radius of the Ni^{3+} species in 8-fold coordination (0.56 Å) are smaller than the Fe^{3+} (0.645 Å) one [25].

The H_2-TPR profiles of the different materials are shown in ***Fig 2***. As it has been reported in the literature, the reduction processes into a perovskite system are commonly linked to the B-site cations, since the A-site cations are rather difficult to reduce under experimental conditions [26,27]. A complex profile divided in two regions (*region I* and *II*) can be distinguished for the support and the catalytic systems. Regarding the LSCF reduction profile, the *region I* and *II* have been widely associated to Co^{3+} and Fe^{3+} reduction, respectively [23,26,28]. The former is observed at low temperature, between 250-550 ºC, and the latter at higher one, from 700 ºC to 950 ºC. Two main peaks located at maximum temperatures of 380 ºC and 487 ºC were noted in the *region I*, being commonly associated to the next two reduction steps [29,30]: (1) $Co^{3+} \rightarrow Co^{2+}$ and (2) $Co^{2+} \rightarrow Co^{0}$. One single peak at high temperature (around 850 ºC) linked to the reduction of Fe^{3+} to Fe^{0} is detected in the *region II* [23,27,28]. These high reduction temperature has been associated to the high stability of Fe^{3+} in the octahedral sites of a perovskite structure [27]. In addition, the absence of H_2 consumption between the two regions, around 550-700 ºC, indicates the formation of a stable partially reduced cobalt-perovskite (Co^0/LSCF) at this temperature range. Bedel *et al.* [23] proved the formation and stability of partially reduced Co in the orthorhombic $LaCo_xFe_{1-x}O_3$ perovskite between 500-570 ºC under reducing conditions. Similar to our TPR profiles, they found two reduction zones well separated, with no H_2 consumption over the range of temperature aforementioned. In order to elucidate the formation of metallic cobalt on the surface, they followed the reduction by magnetic measurements. For orthorhombic systems ($x < 0.5$), two signals were found at 410 and

625 ºC. The first increase observed at 410 ºC was linked to the ferromagnetic phase formed after the partial reduction of cobalt, giving rise to a metal phase well dispersed on a stable cobalt-deficient perovskite. Recently, Lim et al. [31] have demonstrated that the incorporation of a second transition metal (Ni) into the B-site of $LaCoO_3$ lowered the interaction between La and Co. Thereby, by inserting Ni into $LaCoO_3$, they evidenced that the diffusion from the bulk to the surface is highly feasible under reducing atmosphere for the B-site elements with weaker interaction, forming an ex-solved bimetallic NiCo alloy at the surface. Similarly, a weak interaction between the A-site and B-site caused by the presence of both Fe and Co in the B-site of LSCF structure might favor the migration of part of Co to the surface at reduction temperatures between 550-700 ºC, since Fe ions are reduced at high temperatures. It could explain the formation of this partially reduced Co-perovskite. Nevertheless, in view of the complexity of the system, deep investigations must be conducted to describe in detail this phenomenon. The impregnated catalyst, Ni/LSCF, and bare support exhibit similar reduction profile. The likely presence of the secondary $LaNiO_3$ phase for the Ni/LSCF catalyst prior discussed in the XRD results gives an even more complex reduction process than for the bare LSCF oxide. Likewise, two peaks centered at temperatures close to those above mentioned (385 ºC and 476 ºC) are perceived for Ni/LSCF in the *region I*, with a small one placed at the lowest temperature, 290 ºC. Two reduction peaks have been reported in the literature for the complete reduction of the $LaNiO_3$ perovskite [1,32]. The first reduction peak, located at low temperatures (350-450 ºC), was ascribed to the reduction of $LaNiO_3$ to Ni^0 and the formation of the La_2NiO_4 spinel. Afterwards, the spinel phase could be further reduced, resulting in the complete reduction of Ni^0 and the formation of La_2O_3 [32]. This second reduction process usually appears at higher temperatures (~530-550 ºC). Accordingly, the peak located at the lowest temperature might be attributed to the reduction of the "free"

NiO to Ni^0 with weak Ni-support interaction, not observed by XRD analysis for the Ni/LSCF catalyst (***Fig 1***). The two other peaks found in the *region I* could be associated to the decomposition of the $LaNiO_3$ perovskite along with the reduction of Co^{3+} species. Indeed, the simultaneous reduction of $LaNiO_3$ and of Co^{3+} species can be evidenced by the noticeable increase in the H_2 consumption into the *region I* attained for Ni/LSCF. As expected, the addition of Ru lowers the temperature of the *region I* compared to the Ni/LSCF catalyst and notably enhances the H_2 consumption of the peak located at the lowest temperature as well. . It suggests that Ni reduction is promoted by the addition of Ru over the Ni/LSCF catalyst. Regarding the Ni-LSCF catalyst, the *region I* is shifted to higher temperatures and shows a distinct profile shape compared to the impregnated Ni/LSCF catalyst and the bare LSCF oxide, presumably due to the presence of inserted Ni ions species into the LSCF oxide. This shift might hint that the interaction between the A-site and B-site ions or between the transition metals in the B-site is strong and it could hinder in some extent the migration of metallic Co at the surface. The main reduction peak observed at 460 ºC could be mostly related to the reduction of Ni species to Ni^0 with strong Ni-support interaction [33,34]. Different shoulder peaks most likely linked to the Co^{3+} and Ni^{3+} reduction can be as well distinguished in this zone. The shift of the *region II* to lower temperature in both Ni- and RuNi-containing materials with respect to the support reveals that the support reduction is favored by the presence of (Ru)Ni added. This shift is noteworthy for the Ni-LSCF catalyst compared to Ni/LSCF, suggesting that inserted Ni^{2+} species into the LSCF structure might provide high removable oxygen species.

Furthermore, the support reducibility is reported in ***Table 1*** for the prepared materials. As it can be seen, the Ni addition enhances the support reducibility, increasing from 29% to 54% for Ni/LSCF catalyst and up to 72% for Ni-LSCF one. No modification in the

support reducibility is displayed for the RuNi/LSCF catalyst (56%) compared to the Ni/LSCF one (54%). Therefore, the enhancement of the support reducibility is remarkable for the Ni-LSCF catalyst due to the partial Ni insertion into the LSCF oxide, while the presence of Ru promotes the Ni reduction, but does not improve the support reducibility.

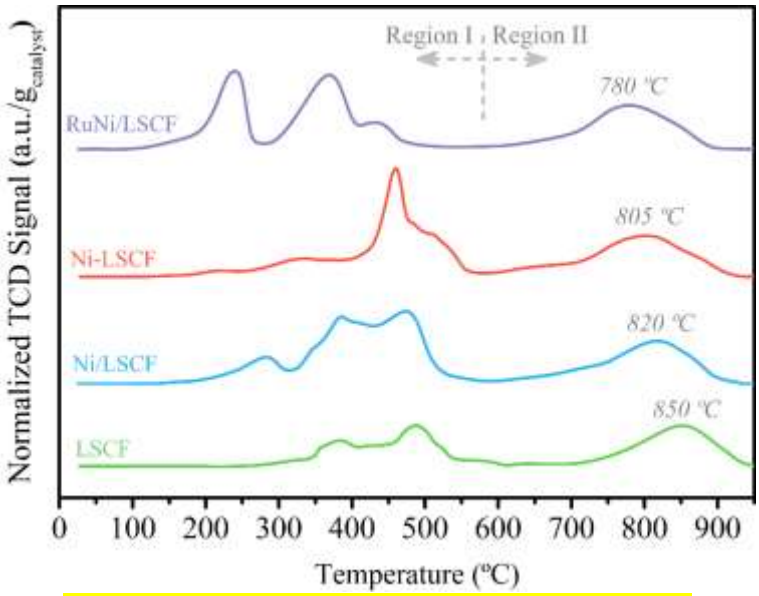

Fig 2. *H_2-TPR profiles of the prepared materials*

The H_2-TPD profiles of all the prepared catalyst are shown in ***Fig 3.*** Two main peaks with different relative intensities, located at 124 ºC and 386 ºC, are displayed for the four investigated materials. These peaks are respectively ascribed to a weakly and strongly adsorbed H species on reduced cobalt, according to Gonzalez Tejuca *et al.* [35]. The presence of these Co species partially reduced at 600 ºC proves the formation of a pseudo stable state (Co^0/LSCF) between 550-700 ºC temperature range, prior evidenced by H_2-TPR analysis for all the prepared materials (***Fig 2***). An increase in the intensity of the peak at high temperature is shown for the impregnated catalysts, being more noticeable for the Ru-containing catalyst (RuNi/LSCF). This enhancement highlights the promotion of the cobalt reduction by the presence of Ni species, as it has been previously seen by H_2-TPR. Moreover, the increased intensity of the peak at the lowest temperature (~124

ºC) displayed for the RuNi/LSCF catalyst might be due to the generation of metallic Ru species. By contrary, these peaks are less intense for the sol-gel catalyst, Ni-LSCF, compared to the Ni/LSCF one and the bare LSCF mixed oxide, revealing that the amount of the reduced Co and Ni species generated at the surface are much lower than for its equivalent impregnated catalyst. It confirms that the Ni insertion enhances the interaction of the Co cations either with the A-site cations (La, Sr) or with the other B-site cations (Ni, Fe), inhibiting the migration from the bulk to the surface of these species along with the metallic Ni ones. Indeed, this fact it has been evidenced by the metallic surface area, reported in ***Table 1*** for the Ru(Ni)-containing catalysts. In general, low values of metallic surface area are displayed for all the catalysts as consequence of the low SSA shown for the LSCF mixed oxide. A rather lower metallic surface is attained for Ni-LSCF (0.5 $m^2 \cdot g^{-1}$) than for Ni/LSCF (1.9 $m^2 \cdot g^{-1}$), most likely due to the large NiO particle size initially displayed for the Ni-LSCF catalyst (26 nm) estimated from XRD analysis (***Table 1***). As well, the strong interaction between Co and A-site cations or the other B-site cations into the lattice of the LSCF oxide observed for the Ni-LSCF catalyst might hamper the diffusion of these species through the bulk to the surface. The reduction of the low amount of "free" NiO as well as the probable decomposition of the $LaNiO_3$ perovskite to Ni^0 and La_2O_3 could generate small Ni^0 particles size, enhancing the metallic surface for the Ni/LSCF catalyst. The metallic surface was alike for both impregnated catalysts, Ni/LSCF (1.9 $m^2 \cdot g^{-1}$) and RuNi/LSCF (2.1 $m^2 \cdot g^{-1}$), which is in accordance with the support reducibility reported in ***Table 2***.

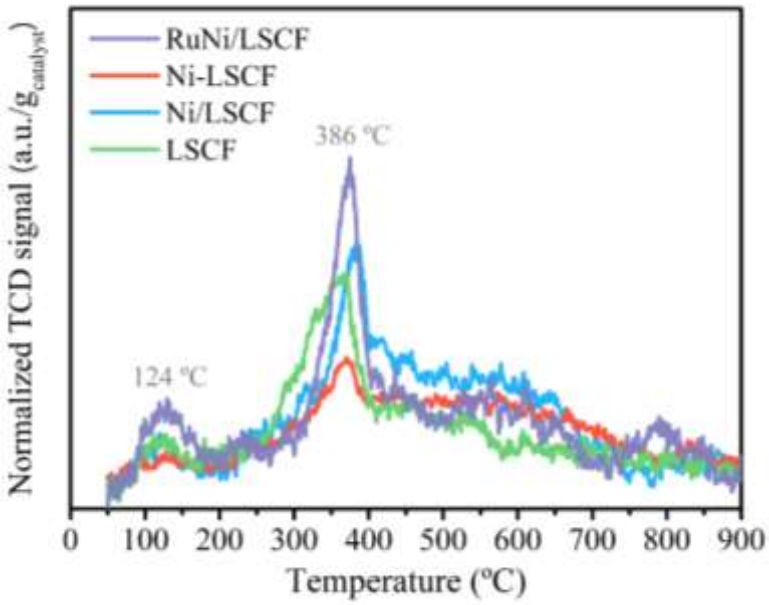

Fig 3. *H_2-TPD profiles of the prepared materials after reduction at 600 ºC for 2 h under H_2/Ar atmosphere*

The XPS spectra of Ni 2p – La 3d regions are presented in ***Fig 4***. The analysis of these regions (***Fig 4***) becomes complicated due to the partial overlapping of the Ni 2p and the La 3d photoelectron peaks. Peaks located at binding energies (BE) between 845 eV and 830 eV, linked to the $3d_{3/2}$ and $3d_{5/2}$ orbital components of the La^{3+} state, are found for all the as prepared materials (***Fig 4***)[36,37]. Additional remaining peaks in the BE region of 870-840 eV related to the satellite peaks of La^{3+} species can be also discerned [36]. The appearance of such as satellite peaks as well as their relative intensity and binding energy separation are highly susceptible to the chemical coordination environment of the La atoms, giving rise to complex spectra [36,38]. As expected, differences in intensity between the Ni/LSCF and Ni-LSCF catalysts are noticeable within the Ni 2p region (875-840 eV) (***Fig 4)***. The $2p_{1/2}$ and $2p_{3/2}$ orbital components associated to the Ni species can be clearly evidenced for the Ni/LSCF catalyst. Peaks placed at 853.4 eV and 860.3 eV, ascribed to the $2p_{3/2}$ orbital component and its satellite peak, as well as the $2p_{1/2}$ satellite peak found at 873.6 eV, are distinctive of the Ni^{2+} species and verifies the presence of the "free" NiO species at the surface of the Ni/LSCF catalyst [39]. Besides, two peaks located

at 854.8 eV and 853.4 eV can be deduced for this latter material in the overlapping region (***inset Fig 4)***. Similar XPS spectra shape has been observed within this region in the literature, where peaks around 855.5 eV and 853.8 eV have been widely linked to Ni^{3+} and Ni^{2+} species, respectively [39,40]. It must be remarked that XPS analysis cannot be used as a definitive proof of the existence of the $LaNiO_3$ perovskite for the Ni/LSCF catalyst since Ni^{2+} and Ni^{3+} are difficult to discriminate, especially considering the overlapping of the La 3d and Ni $2p_{3/2}$ peaks (***Fig 4***). Despite that, the highly probable Ni^{2+}/Ni^{3+} mixture at the surface deduced by XPS along with the prior results obtained by XRD and H_2-TPR could suggest the formation of $LaNiO_3$ as a secondary perovskite for the Ni/LSCF catalyst. The absence of Ni-related peaks in the Ni 2p region of the Ni-LSCF spectrum, even though similar Ni content as Ni/LSCF is expected (~ 13 wt%, ***Table 1***), points out that the nickel atoms are fully inserted in the bulk of the LSCF structure. This fact could explain the low metallic surface area of Ni-LSCF (***Table 2***) and highlights, once again, that the Ni^{2+} insertion into the LSCF structure is promoted by the sol-gel method, in accordance with XRD and H_2-TPR results.

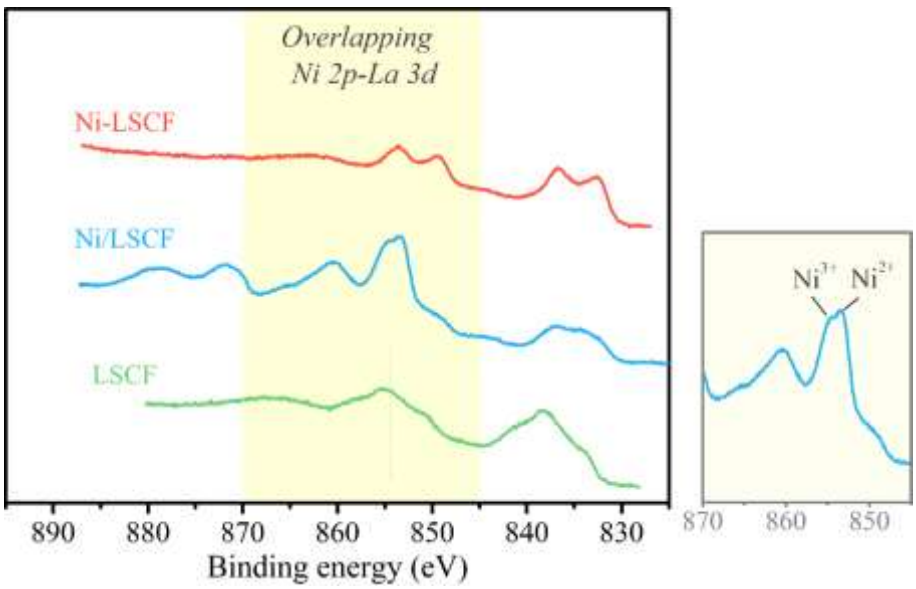

Fig 4. *XPS spectra of La 3d – Ni 2p region of the prepared materials*

XPS spectra of Co 2p and Fe 2p regions are plotted in ***Fig 5*** for the materials of this study. The Mg K_α irradiation was also used for the Ni/LSCF spectrum (see ***insets, Fig 5***) in order to remove the interferences of the Auger Ni (LMM) peak which falls into both regions when the samples are irradiated with Al K_α irradiation. Regarding the Co 2p region, one peak around 782.3 eV and small shoulder at 787.3 eV can be discerned for all the materials (***Fig 5 (a)***), ascribed to the component $2p_{3/2}$ of different cobalt ions (Co^{2+}, Co^{3+} or Co^{4+}) [41]. The oxidation state of these cobalt species is quite difficult to identify because of the proximity of the Co^{2+} and Co^{3+} peaks [42]. Generally, photoelectron peaks around 725.4 eV and 711.9 eV belong to the Fe^{3+} species are discerned in the Fe 2p region for all the investigated materials (***Fig 5 (b)***) [41].

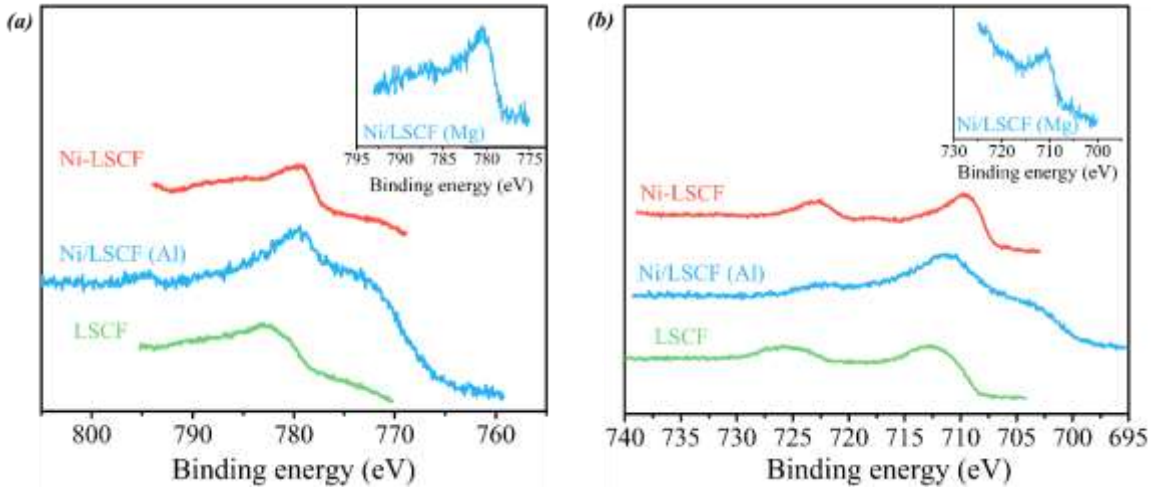

Fig 5. *XPS spectra of* ***(a)*** *Co 2p and* ***(b)*** *Fe 2p regions of the prepared materials.*

The chemical surface composition determined by XPS spectra is shown in ***Table 3*** for the prepared materials. The region areas linked to the La $3d_{5/2}$ orbital components (from 845 to 830 eV) have been considered to calculate the La surface content. Moreover, the Ni surface content was just reported for the Ni/LSCF catalyst since the Ni $2p_{1/2}$ peaks were not noticeable within the Ni 2p region for the Ni-LSCF one (***Fig 4 (a)***). Some differences in the surface composition compared to the bulk are found for the bare LSCF. The higher La content achieved at the surface compared to

the bulk for the bare LSCF is consistent with the presence of the La_2O_3 phase earlier detected by XRD analysis. As expected, a Ni content slightly higher than in the bulk is found at the surface for the Ni/LSCF catalyst, giving rise to a noteworthy decrease of the La and Sr content compared to the bulk composition and to the surface content of the bare LSCF. The likely formation of $LaNiO_3$ could also cause the decrease in the La surface content for the Ni/LSCF catalyst. Similarly, lower La content is displayed for the Ni-LSCF (29.5 at %) compared to the bare LSCF, outstanding that the La insertion into the perovskite structure is encouraged by the Ni insertion. Thereby, the formation of the La_2O_3 phase is less favored through sol-gel method and, it explains its non-detection by XRD analysis for the Ni-LSCF catalyst (see ***Fig 1***). In addition, a higher Sr (30.0 at %) at the surface is achieved for Ni-LSCF catalyst than for the bare LSCF (17.3 at %) and the Ni/LSCF catalyst (5.4 at %). Due to its basic character, this high content of Sr shown for the Ni-LSCF catalyst might facilitate the steam adsorption at the surface under steam reforming conditions. The low amount of Co and Fe found for the Ni-LSCF compared to the Ni/LSCF at the surface is in good agreement with the low metallic surface attained for the former catalyst (***Table 2***).

Table 3*. Chemical surface composition calculated by XPS, and bulk composition calculated by XRF in brackets (without oxygen) for the prepared materials*

	La (at %)	***Sr (at %)***	***Co (at %)***	***Fe (at %)***	***Ni (at %)***
LSCF	34.9 [26.2]	17.3 [24.6]	17.5 [12.2]	30.4 [37.0]	-
Ni/LSCF	8.2 [19.5]	5.4 [20.9]	21.4 [9.7]	40.8 [29.2]	24.2 [20.7]
Ni-LSCF	29.5 [19.1]	30.0 [18.8]	19.7 [11.0]	20.8 [29.6]	- [21.7]

3.2.Catalytic activity

Prior the catalytic tests, all the samples have been submitted to a reduction pretreatment at 600 ºC for 2 h under 40 %mol H_2/N_2 mixture. According to H_2-TPR and H_2-TPD, the formation of a Co^0/LSCF perovskite are expected for all the materials. In addition, part of the $LaNiO_3$ phase observed for the (Ru)Ni/LSCF catalysts could be: (i) fully reduced, generating Ni^0 species and La_2O_3 or (ii) partially reduced, generating Ni^0 and a secondary La_2NiO_4 spinel phase.

In the present study, steam reforming of toluene and phenol at 550 ºC for 6 h has been conducted over the prepared materials.

The steam reforming of toluene could proceed as described in *Reaction 1*. Additionally, hydrogenation of toluene can simultaneously occur (*Reaction 2*), giving benzene as by-product.

$$C_7H_8 + 7\,H_2O \rightarrow 7\,CO + 11\,H_2 \qquad \textit{Reaction 1}$$

$$C_7H_8 + H_2 \rightarrow C_6H_6 + CH_4 \qquad \textit{Reaction 2}$$

The steam reforming of phenol is described as follows:

$$C_6H_5OH + 5\,H_2O \rightarrow 6\,CO + 8\,H_2 \qquad \textit{Reaction 3}$$

Besides the steam reforming reactions, other parallel equilibrium reactions such as WGS (*Reaction 4*), CO methanation (*Reaction 5)* and/or carbon formation through Boudouard reaction (*Reaction 6*) or thermal decomposition of the tar model molecule can take place.

$$CO + H_2O \leftrightarrow CO_2 + H_2 \qquad \textit{Reaction 4}$$

$$CO + 3H_2 \leftrightarrow CH_4 + H_2O \qquad \textit{Reaction 5}$$

$$2CO \leftrightarrow C^* + CO_2 \qquad \textit{Reaction 6}$$

The partial molar flows of the gaseous components (H_2, CO, CO_2 and CH_4) versus time on stream during toluene and phenol reaction can be respectively found in ***Fig 6*** and ***7***. Moreover, the average tar conversion, the selectivity to benzene (for toluene reforming) and to coke formation are reported in ***Table 4***. As the bare LSCF support are composed

by transition metals, such as Co and Fe, likely actives in steam reforming reactions, its catalytic activity has been evaluated in toluene reforming. The changes in the outlet partial molar flows under both model molecules, toluene (***Fig 6***) and phenol (***Fig 7***), follow similar trend for the bare support and the (Ru)Ni-containing materials. Thus, the CO consumption along with the CO_2 and CH_4 production indicate that WGS and CO methanation are the main reactions that simultaneously occur. The slight amount of CH_4 formed compared to CO_2 observed in both reforming reactions (***Fig 6*** for toluene and ***Fig 7*** for phenol) for all the investigated materials highlights that a considerably higher catalytic activity toward WGS reaction than CO methanation are achieved. This observation could be due to the presence of Co or Fe into the bare LSCF structure, well-known to be active in WGS reaction [43]. In addition, it has been reported that a high density of active hydroxyl species could enhance the catalytic activity toward WGS instead of CO methanation by generating reaction intermediates [44]. According to Zhang *et al.* [45], the basic character of Sr, present into the bare LSCF structure, could facilitate the water adsorption and enhance the content of active OH groups, promoting in that case the WGS reaction. Hence, the presence of Sr into the LSCF perovskite could also favored the WGS reaction instead of the CO methanation for these types of materials in both toluene (***Fig 6***) and phenol reforming (***Fig 7***) conditions.

As far as the influence of the preparation method is concerned, stable partial molar flows along the time on stream can be found for all the prepared materials, regardless the tar model molecule, (***Fig 6*** for toluene and ***Fig 7*** for phenol). The catalytic activity toward the WGS reaction seems to be alike for the bare LSCF and the impregnated Ni/LSCF catalyst during toluene reforming, whereas the sol-gel Ni-LSCF shows the highest catalytic activity to WGS among the prepared materials in both reforming reactions. No enhancement in apparent catalytic activity due to the addition of Ru is displayed for the

RuNi/LSCF with respect to the Ni/LSCF catalyst, as it can be seen from their outlet molar flows (***Fig 6*** and ***7***).

As regards the average toluene conversion (***Table 4***), no significant catalytic activity to toluene reforming is shown for the bare LSCF, with a toluene conversion less of 5%. Slightly higher toluene conversion (65%) and resistance to coke formation (S_{coke} of 7%) is exhibited for the Ni-LSCF than for the Ni/LSCF catalyst ($X_{toluene}$ of 54% and S_{coke} of 16%). Both the catalytic activity toward toluene reforming and the resistance to coke formation are improved by the addition of Ru over Ni/LSCF catalyst. Thus, the toluene conversion becomes 82% from 54% as well as the selectivity to carbon decreases from 16% to 8%. Generally, the selectivity to benzene is negligible for all the prepared materials (~2 – 4%).

Concerning the average phenol conversion, comparable values are attained for both Ni/LSCF and Ni-LSCF catalysts (~85 – 90%). Similarly, the Ni/LSCF catalyst (S_{coke} of 15%) displays lower resistance to coke formation than the Ni-LSCF one (S_{coke} of 9%) (***Table 4***). Despite the high carbon selectivity achieved for the Ni/LSCF catalyst, the high stability displayed in the gas phase along the reforming reactions for both tar molecules should be highlighted, accounting for an apparent stable catalytic activity. An opposite behavior in the catalytic activity is exhibited for the RuNi/LSCF catalyst in phenol reforming reaction, reaching similar average phenol conversion (76%) and selectivity to carbon (16%) as Ni/LSCF.

As expected from the inlet tar content, a higher average tar conversion is achieved for phenol ($WHSV_{tar}$ of 1.4 h^{-1} and S/C_{tar} of 16.5) than for toluene reforming ($WHSV_{tar}$ of 2.6 h^{-1} and S/C_{tar} of 7.7) for the three materials of the study. However, the selectivity to carbon achieved for the prepared materials is alike under both reforming reactions, even though the reactions conditions were softer for phenol than for toluene reforming. This

fact, along with the differences in catalytic activity toward tar reforming shown for RuNi/LSCF, highlights the differences in the reaction mechanism between oxygenate and hydrocarbon compounds. These results are in good agreement with those achieved in prior study, beingassociated to the low thermal stability of the oxygenate compounds that could easily undergo through thermal decomposition and/or cracking over the support [3]. Therefore, high amount of coke at the catalyst surface due to phenol decomposition might be able to be generated, despite the high-water content used.

Broadly, the catalytic stability regarding the gas phase analysis and the catalytic activity toward tar reforming displayed for both Ni-containing materials are alike, being Ni/LSCF more prone to carbon formation than Ni-LSCF. Thus, taking into account the catalytic activity to WGS displayed in the gas phase as well as the resistance to coke formation, it could be concluded that the sol-gel Ni-LSCF catalyst is the best catalytic system of the series.

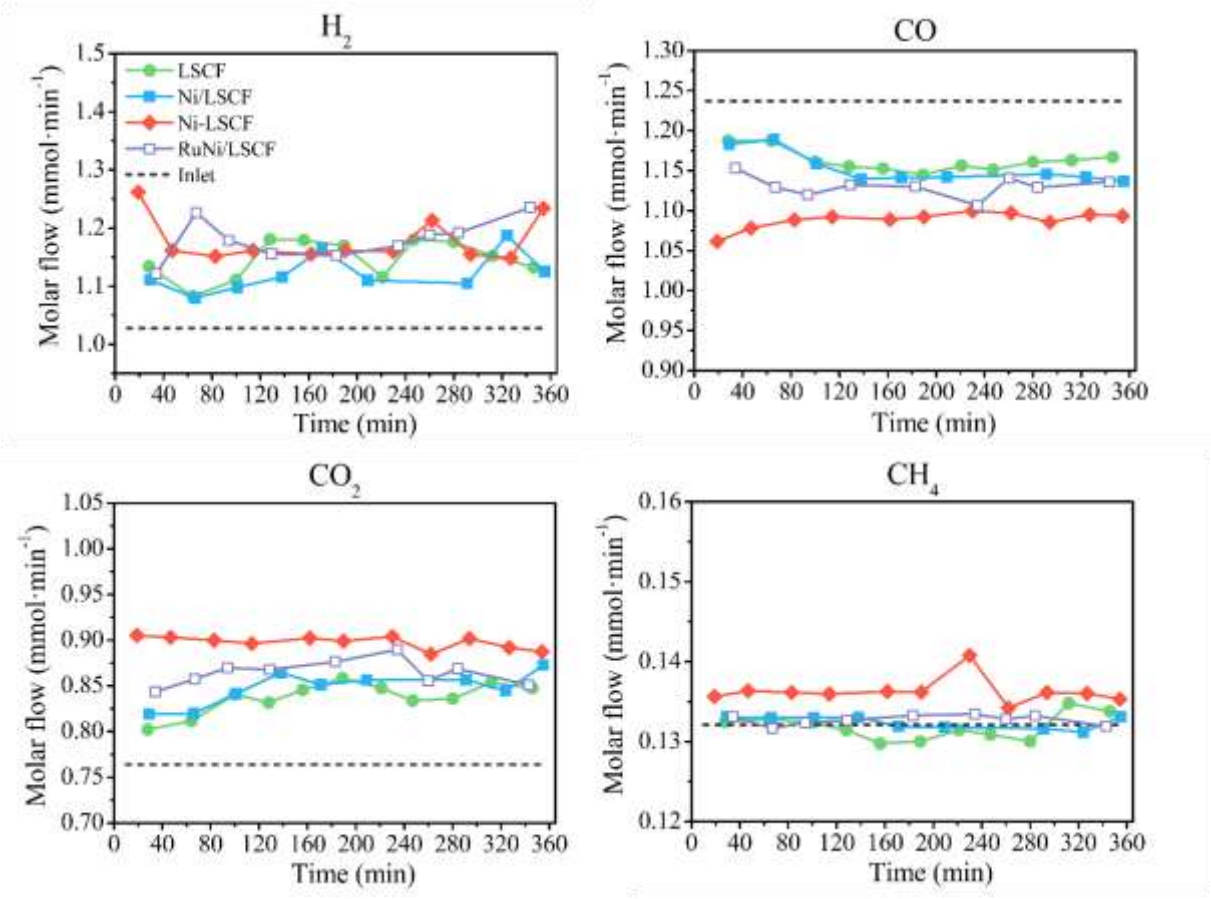

Fig 6. *Outlet partial molar flows vs time on stream during toluene reforming at 550 ºC over the prepared catalysts ($WHSV_{gas}$ = 370 h^{-1}; $WHSV_{tar}$ = 2.6 h^{-1} and S/C_{tar} = 7.7).*

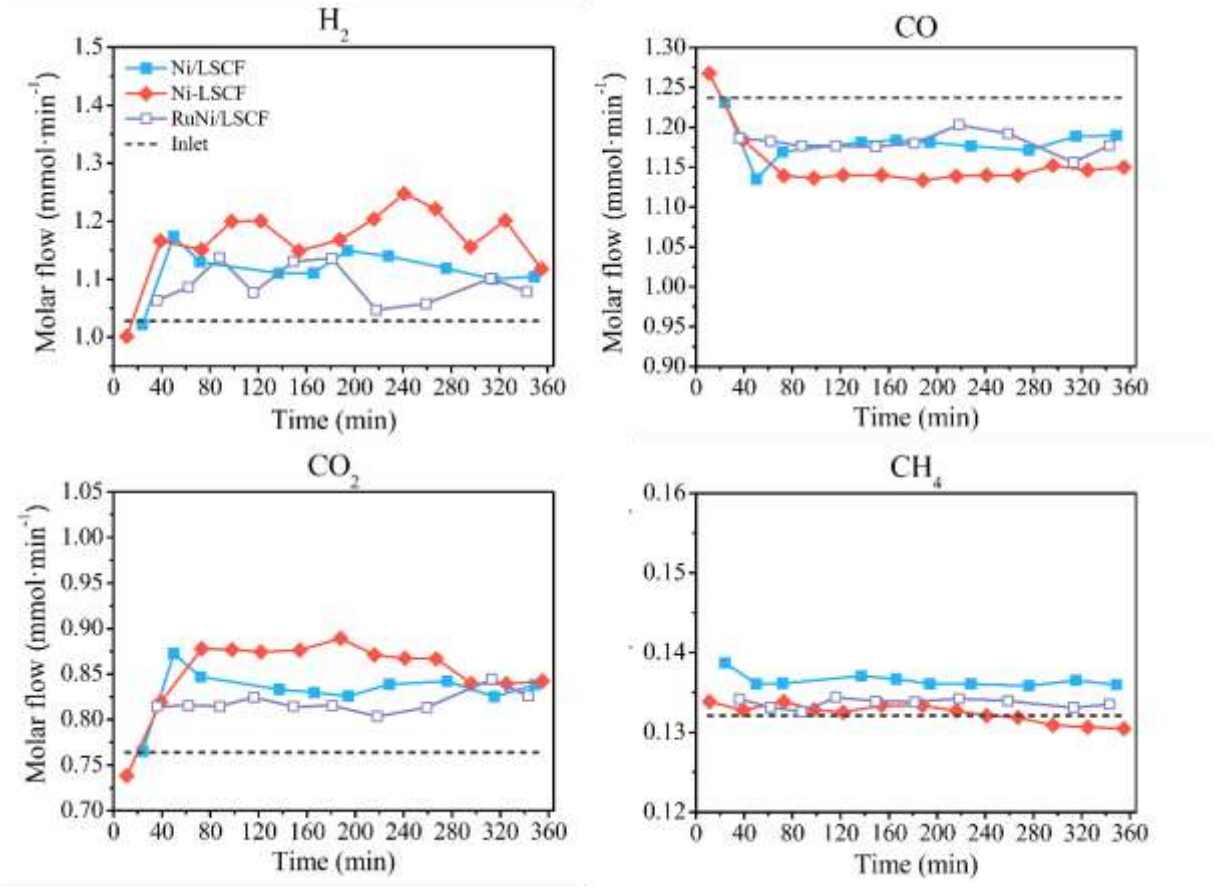

Fig 7. *Outlet partial molar flows vs time on stream during phenol reforming at 550 ºC over the prepared catalysts ($WHSV_{gas}$ = 370 h^{-1}; $WHSV_{tar}$ = 1.4 h^{-1} and S/C_{tar} = 16.5).*

Table 4. *Average tar conversion, selectivity to benzene (for toluene reforming) and selectivity to carbon for steam reforming of toluene and phenol at 550 ºC*

Model tar molecule	*Toluene*			*Phenol*	
	$X_{toluene}$ (%)	$S_{benzene}$ (%)	S_{coke} (%)	X_{phenol} (%)	S_{coke} (%)
LSCF	< 5	-	-	-	-
Ni/LSCF	54	4	16	85	15
Ni-LSCF	65	2	7	90	9
RuNi/LSCF	82	< 2	8	76	16

The key role of the metallic surface in reforming reactions have been underlined in prior studies [3,46,47]. It has been demonstrated that the catalytic activity is correlated with the metallic surface for a given catalyst. However, a similar catalytic activity toward steam

reforming reactions was attained for both Ni-containing catalyst, despite the rather higher metallic surface found by H_2-TPD analysis for Ni/LSCF (1.9 $m^2 \cdot g^{-1}$) than for Ni-LSCF (0.5 $m^2 \cdot g^{-1}$). This comparable catalytic behavior might be associated to the fact that the active phase (Ni) forms part of a perovskite structure for both fresh catalysts as $LaNiO_3$ phase for Ni/LSCF and as Ni^{2+} partially inserted into LSCF for Ni-LSCF, according to XRD and XPS results. Regarding the resistance to coke, several researchers underlined the positive effect of Sr in reforming reactions owing to its basicity. The catalyst surface basicity is known to inhibit coke formation in dry reforming of methane[48] and steam reforming of n-heptane[49] by enhancing the water adsorption and, thereby the carbon gasification on the catalyst surface. Moreover, it was observed that the substitution of La with Sr atoms into a La-based perovskite structure upgrades the lattice oxygen mobility at the surface of the Ni/$La_{0.7}Sr_{0.3}AlO_{3-\delta}$ catalyst, leading to high resistance to coke deposits[20]. Accordingly, the higher resistance to coke formation shown for Ni-LSCF than for Ni/LSCF could be due to the higher Sr content at the surface displayed for the former(30.0 at %) compared to the latter (5.4 at %), that can promote the carbon gasification by facilitating the water adsorption. This could be also ascribed to the high lattice oxygen mobility suggested by the shifts to lower temperature of the *region II* for Ni-LSCF than for Ni/LSCF through H_2-TPR analysis (see ***Fig 2***). Furthermore, it has been reported in the literature that an increase in the amount of Fe into a catalytic system enhances the acidity of the catalyst surface[50]. Therefore, the high Fe content along with the low Sr content found by XPS analysis at the surface of Ni/LSCF catalyst (***Table 3***) could provoke an increase in the acidity of the catalyst surface. Consequently, catalytic tar cracking reactions might be more favoured, leading to a higher amount of coke deposits in the case of this catalyst. Eventually, as the physicochemical properties are alike for both Ni/LSCF and RuNi/LSCF, the better catalytic activity achieved for the

latter in toluene reforming points out the positive impact of Ru as noble metal. However, this improvement was not noticeable in phenol reforming conditions (at high S/C_{tar}), attaining slightly lower average phenol conversion and similar selectivity to coke to the bare Ni/LSCF catalyst (see ***Table 4***).

Steam reforming of toluene has been performed over similar kinds of materials using toluene/steam mixture as a feedstock at reaction temperatures around 550-650 ºC. Sekine *et al.*[20] investigated the catalytic activity toward toluene reforming reaction ($WHSV_{tar}$= 0.81 h^{-1}, S/C_{tar}= 2) over 10 wt% Ni/$La_{0.7}Sr_{0.3}AlO_3$ catalyst at 600 ºC for 180 min, achieving a toluene conversion of 57%. Oemar *et al.*[19] found a toluene conversion of 48% for a perovskite composed by $La_{0.8}Sr_{0.2}Ni_{0.8}Fe_{0.2}O_3$ after 500 min on stream under toluene reforming reaction ($WHSV_{tar}$= 34.6 h^{-1} , S/C_{tar}= 3.4) at 650 ºC. More recently, Zhang *et al.*[45] reported a toluene conversion of 65% and 93% for 9 wt% Ni/$La_{0.7}Sr_{0.3}AlO_3$ when toluene reforming ($WHSV_{tar}$= 1.33 h^{-1} ,S/C_{tar}= 2) was performed for 120 min at reaction temperatures of 550 ºC and 650 ºC, respectively. To the best of our knowledge, research studies that investigate steam reforming of toluene under model syngas composition were not reported yet in the literature for these Ni-perovskite type systems. Besides, studies dedicated to the catalytic evaluation of these type of materials under reforming reaction using phenol as model tar molecule have not been found either, not even employing phenol/steam mixture as feedstock. In the present study, average toluene conversion around 55-65% was obtained for Ni-based catalysts (Ni/LSCF and Ni-LSCF) using lower temperature than generally reported and a mixture of a model syngas composition and toluene as tar. It reveals the high efficiency toward toluene reforming of the investigated catalysts.

Even if no comparison with data from literature is possible, the high average phenol conversion (85%) found for these materials under severe conditions in this work must be highlighted, contributing new and innovative results.

4. Characterization of spent catalysts

Diffractograms of the spent catalysts after reforming reactions can be found in ***Fig 8.*** Regardless the model tar molecule, no modifications in the crystalline structure of the LSCF perovskite after the catalytic tests is observed for the spent materials compared to the fresh ones. Generally, peaks located at 2θ ~ 44º and 52º ascribed to the metallic Ni phase are evidenced for all the spent materials. The La_2O_3 phase, expected from the complete reduction of $LaNiO_3$ phase, is not noticeable for the impregnated (Ru)Ni/LSCF catalysts (***Fig 8 (a) and (c)***), despite the formation of Ni^0 due to the reduction pretreatment. Therefore, the existence of Ni as a $LaNiO_3$ perovskite or as a La_2NiO_4 spinel structure could be assumed for the (Ru)Ni/LSCF catalysts, elucidating the similar catalytic behavior found for both Ni/LSCF and Ni-LSCF catalysts. Eventually, a peak belonging to the NiO phase is barely discerned for all the spent catalysts likely due to the re-oxidation of the Ni^0 in atmosphere or its oxidation with the steam or with the lattice oxygen of the catalytic support[3]. It reveals that catalytic deactivation by Ni oxidation is negligible, clarifying the high catalytic stability observed in the gas phase for all the catalysts. An additional peak placed around 2θ ~ 26º displayed for the spent materials indicates the formation of structural or graphitic carbon during the steam reforming reactions.

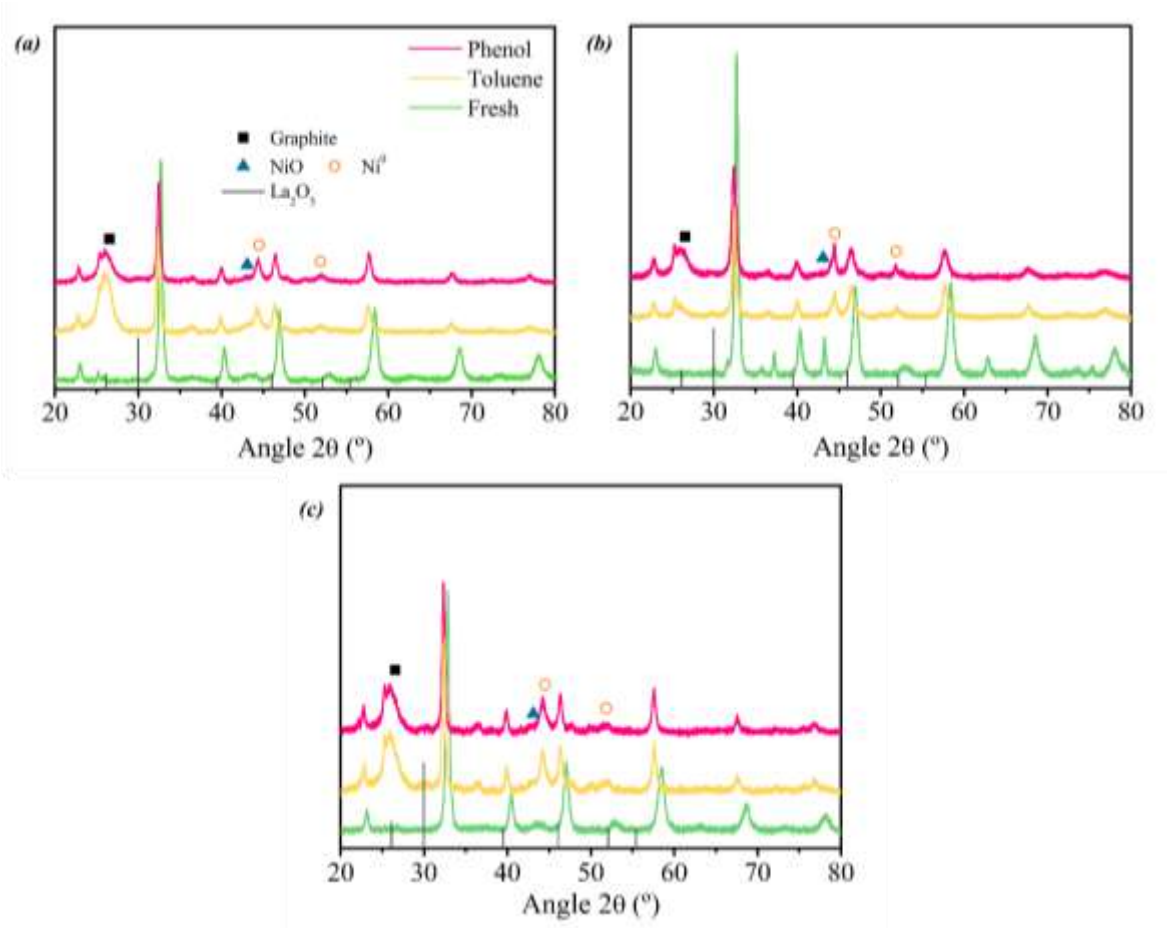

Fig 8. *Diffractogram of spent materials post-steam reforming reactions: (a) Ni/LSCF, (b) Ni-LSCF and (c) RuNi/LSCF*

The morphology of the carbon deposits generated over the catalysts surface during steam reforming reactions has been also studied. ***Fig 9*** shows the SEM image of the spent Ni/LSCF catalyst post-toluene reforming reaction. Structural carbon deposits as carbon nanofibers are mainly found, as prior observed by XRD of the spent materials. The formation of this type of carbon deposit might be favored by the presence of the CO_2 and the CH_4 in the inlet syngas composition, widely used as precursors of carbon nanofibers or nanotubes in Catalytic Chemical Vapor Deposition processes[3,51].

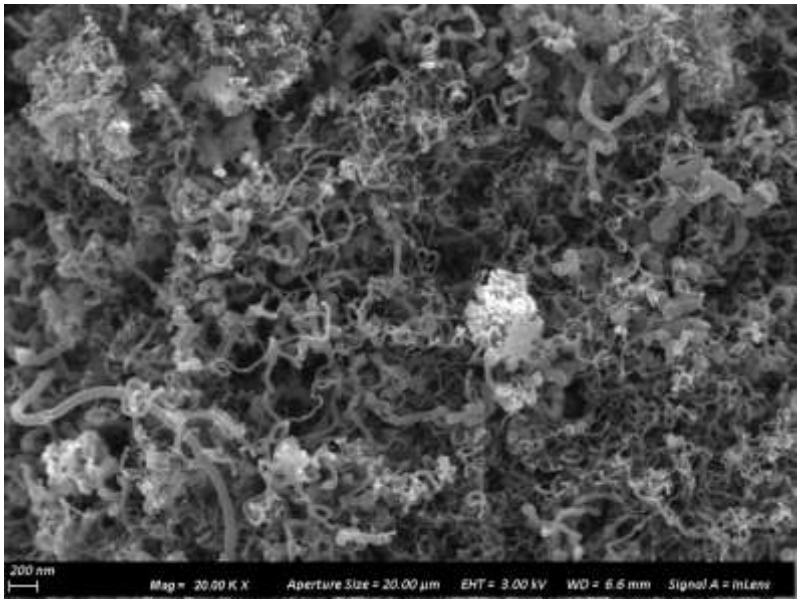

Fig 9. *SEM image of the Ni/LSCF catalyst post-toluene reforming reaction*

5. Conclusions

In the present work, two different preparation methods were used for the synthesis of the (Ru)Ni-LSCF systems, wetness impregnation and pseudo sol-gel, giving rise to (Ru)Ni/LSCF and Ni-LSCF catalysts, respectively. Accordingly, the influence of the preparation method as well as the presence of Ru as noble metal on the physicochemical properties and the catalytic activity toward steam reforming reactions was studied.

Steam reforming of tar using toluene and phenol as model tar molecule along with a typical syngas composition has been conducted over all the catalysts of the study. No influence of the synthesis path on the catalytic activity toward tar reforming was observed. Thus, regardless the model tar molecule, similar average tar conversion and stability in the gas phase was found for both Ni/LSCF and Ni-LSCF catalysts due to the presence of Ni as perovskite structure in both systems. The higher catalytic activity to WGS and resistance to coke formation found for the Ni-LSCF catalyst than for the Ni/LSCF one has been ascribed to the presence of high removable oxygen species indicated by H_2-TPR and the higher Sr content found at the surface of this material by

XPS. It stresses out the important role of the surface basicity in the coke formation and therefore, in the likely catalytic deactivation under reforming reaction conditions. An improvement in the catalytic activity toward reforming reaction and in the resistance to coke formation was evidenced for RuNi/LSCF during toluene reforming, whereas no improvement in tar conversion compared to the bare Ni/LSCF was achieved under phenol reforming conditions. This opposite catalytic performance as well as the high selectivity to coke attained for phenol reforming, despite the high S/C_{tar}, highlighted the differences in the reaction mechanism between the two model tar molecules of the study.

Generally, the catalytic results reveal that the studied systems are highly efficient and have a great potential for tar abatement at relatively low temperature under simulated biomass gasification conditions, upgrading the syngas produced.

Acknowledgment

This work has been performed in the framework of Efficient Use of Biomass for Low Emissions Production of Renewable Energy and Biotechnological Valuable Products (EBIPREP) project of the INTERREG IV Rhin Superior program, co-financed by FEDER funds from the European Union – grant nº 3.6.

The XRF analysis provided by Surface Chemistry and Catalysis group (Materials Science Institute of Seville (CSIC)) was greatly appreciated.

The authors thank Dr Corinne Bouillet from IPCMS (Strasbourg) for the TEM analysis.

References

1. Oemar, U.; Ang, P.S.; Hidajat, K.; Kawi, S. Promotional effect of Fe on perovskite LaNixFe 1-xO3 catalyst for hydrogen production via steam reforming of toluene. *Int. J. Hydrogen Energy* **2013**, *38*, 5525–5534, doi:10.1016/j.ijhydene.2013.02.083.

2. Damartzis, T.; Zabaniotou, A. Thermochemical conversion of biomass to second generation biofuels through integrated process design-A review. *Renew. Sustain. Energy Rev.* **2011**, *15*, 366–378, doi:10.1016/j.rser.2010.08.003.
3. Jurado, L.; Papaefthimiou, V.; Thomas, S.; Roger, A. Low temperature toluene and phenol abatement as tar model molecules over Ni-based catalysts: Influence of the support and the synthesis method. *Appl. Catal. B Environ.* **2021**, *297*, 120479, doi:10.1016/j.apcatb.2021.120479.
4. Du, Z.Y.; Zhang, Z.H.; Xu, C.; Wang, X.B.; Li, W.Y. Low Temperature Steam Reforming of Toluene and Biomass Tar over Biochar-Supported Ni Nanoparticles. *ACS Sustain. Chem. Eng.* **2019**, *7*, 3111–3119, doi:10.1021/acssuschemeng.8b04872.
5. Yang, X.; Liu, X.; Guo, T.; Liu, C. Effects of Cu and Fe Additives on Low-Temperature Catalytic Steam Reforming of Toluene Over Ni/AC Catalysts. *Catal. Surv. from Asia* **2019**, *23*, 54–63, doi:10.1007/s10563-018-9260-7.
6. Zeng, X.; Ueki, Y.; Yoshiie, R.; Naruse, I.; Wang, F.; Han, Z.; Xu, G. Recent progress in tar removal by char and the applications: A comprehensive analysis. *Carbon Resour. Convers.* **2020**, *3*, 1–18, doi:10.1016/j.crcon.2019.12.001.
7. Belgiorno, V.; De Feo, G.; Della Rocca, C.; Napoli, R.M.A. Energy from gasification of solid wastes. *Waste Manag.* **2003**, *23*, 1–15, doi:10.1016/S0956-053X(02)00149-6.
8. Guan, G.; Kaewpanha, M.; Hao, X.; Zhu, A.; Kasai, Y.; Kakuta, S.; Kusakabe, K.; Abudula, A. Steam reforming of tar derived from lignin over pompom-like potassium-promoted iron-based catalysts formed on calcined scallop shell. *Bioresour. Technol.* **2013**, *139*, 280–284, doi:10.1016/j.biortech.2013.04.007.
9. Guan, G.; Chen, G.; Kasai, Y.; Lim, E.W.C.; Hao, X.; Kaewpanha, M.; Abuliti,

A.; Fushimi, C.; Tsutsumi, A. Catalytic steam reforming of biomass tar over iron- or nickel-based catalyst supported on calcined scallop shell. *Appl. Catal. B Environ.* **2012**, *115–116*, 159–168, doi:10.1016/j.apcatb.2011.12.009.

10. Guan, G.; Kaewpanha, M.; Hao, X.; Abudula, A. Catalytic steam reforming of biomass tar: Prospects and challenges. *Renew. Sustain. Energy Rev.* **2016**, *58*, 450–461, doi:10.1016/j.rser.2015.12.316.
11. Dayton, D. *Review of the Literature on Catalytic Biomass Tar Destruction: Milestone Completion Report*; Golden, CO, 2002;
12. Ashok, J.; Dewangan, N.; Das, S.; Hongmanorom, P.; Wai, M.H.; Tomishige, K.; Kawi, S. Recent progress in the development of catalysts for steam reforming of biomass tar model reaction. *Fuel Process. Technol.* **2020**, *199*, 106252, doi:10.1016/j.fuproc.2019.106252.
13. Sehested, J. Four challenges for nickel steam-reforming catalysts. *Catal. Today* **2006**, *111*, 103–110, doi:10.1016/j.cattod.2005.10.002.
14. Zhu, H.; Zhang, P.; Dai, S. Recent Advances of Lanthanum-Based Perovskite Oxides for Catalysis. *ACS Catal.* **2015**, *5*, 6370–6385, doi:10.1021/acscatal.5b01667.
15. Oemar, U.; Ang, M.L.; Chin, Y.C.; Hidajat, K.; Kawi, S. Role of lattice oxygen in oxidative steam reforming of toluene as a tar model compound over Ni/La0.8Sr0.2AlO3 catalyst. *Catal. Sci. Technol.* **2015**, *5*, 3585–3597, doi:10.1039/c5cy00412h.
16. Oemar, U.; Ming Li, A.; Hidajat, K.; Kawi, S. Mechanism and kinetic modeling for steam reforming of toluene on La 0.8 Sr 0.2 Ni 0.8 Fe 0.2 O 3 catalyst. *AIChE J.* **2014**, *60*, 4190–4198, doi:10.1002/aic.14573.
17. Ferri, D. Methane combustion on some perovskite-like mixed oxides. *Appl.*

Catal. B Environ. **1998**, *16*, 119–126, doi:10.1016/S0926-3373(97)00065-9.

18. Ponce, S.; Peña, M.A.; Fierro, J.L.G. Surface properties and catalytic performance in methane combustion of SR-substituted lanthanum manganites. *Appl. Catal. B Environ.* **2000**, *24*, 193–205, doi:10.1016/S0926-3373(99)00111-3.
19. Oemar, U.; Ang, M.L.; Hee, W.F.; Hidajat, K.; Kawi, S. Perovskite LaxM1-xNi0.8Fe0.2O3 catalyst for steam reforming of toluene: Crucial role of alkaline earth metal at low steam condition. *Appl. Catal. B Environ.* **2014**, *148–149*, 231–242, doi:10.1016/j.apcatb.2013.10.001.
20. Sekine, Y.; Mukai, D.; Murai, Y.; Tochiya, S.; Izutsu, Y.; Sekiguchi, K.; Hosomura, N.; Arai, H.; Kikuchi, E.; Sugiura, Y. Steam reforming of toluene over perovskite-supported Ni catalysts. *Appl. Catal. A Gen.* **2013**, *451*, 160–167, doi:10.1016/j.apcata.2012.11.005.
21. Natile, M.M.; Ugel, E.; Maccato, C.; Glisenti, A. LaCoO3: Effect of synthesis conditions on properties and reactivity. *Appl. Catal. B Environ.* **2007**, *72*, 351–362, doi:10.1016/j.apcatb.2006.11.011.
22. Ertl G., Knözinger H., Schüth F., W.J. (Eds) *Handbook Of Heterogeneous Catalysis.*; 2nd ed.; Wiley: New York, NY, USA, 2008; ISBN 978-3527312412.
23. Bedel, L.; Roger, A.C.; Estournes, C.; Kiennemann, A. Co^0 from partial reduction of La(Co,Fe)O3 perovskites for Fischer-Tropsch synthesis. *Catal. Today* **2003**, *85*, 207–218, doi:10.1016/S0920-5861(03)00388-2.
24. Sutthiumporn, K.; Maneerung, T.; Kathiraser, Y.; Kawi, S. CO2 dry-reforming of methane over La0.8Sr 0.2Ni0.8M0.2O3 perovskite (M = Bi, Co, Cr, Cu, Fe): Roles of lattice oxygen on C-H activation and carbon suppression. *Int. J. Hydrogen Energy* **2012**, *37*, 11195–11207, doi:10.1016/j.ijhydene.2012.04.059.

25. Shannon, R.D. Revised effective ionic radii and systematic studies of interatomic distances in halides and chalcogenides. *Acta Crystallogr. Sect. A* **1976**, *32*, 751–767, doi:10.1107/S0567739476001551.

26. Ao, M.; Pham, G.H.; Sage, V.; Pareek, V. Structure and activity of strontium substituted LaCoO3 perovskite catalysts for syngas conversion. *J. Mol. Catal. A Chem.* **2016**, *416*, 96–104, doi:10.1016/j.molcata.2016.02.020.

27. Wang, H.; Dong, X.; Zhao, T.; Yu, H.; Li, M. Dry reforming of methane over bimetallic Ni-Co catalyst prepared from La(CoxNi1-x)0.5Fe0.5O3 perovskite precursor: Catalytic activity and coking resistance. *Appl. Catal. B Environ.* **2019**, *245*, 302–313, doi:10.1016/j.apcatb.2018.12.072.

28. Guo, S.; Puleo, F.; Wang, L.; Wu, H.; Liotta, L.F. La0.6Sr0.4Co0.2Fe0.79M0.01O3−δ (M = Ni, Pd) perovskites synthesized by Citrate-EDTA method: Oxygen vacancies effect on electrochemical properties. *Adv. Powder Technol.* **2018**, *29*, 2804–2812, doi:10.1016/j.apt.2018.07.029.

29. Morales, M.; Segarra, M. Applied Catalysis A : General Steam reforming and oxidative steam reforming of ethanol over production. *"Applied Catal. A, Gen.* **2015**, *502*, 305–311, doi:10.1016/j.apcata.2015.05.036.

30. Yakovleva, I.S.; Isupova, L.A.; Rogov, V.A. Oxygen species and their reactivity in the mechanochemically prepared substituted perovskites La1 - X Sr x CoO3 - Y (x = 0-1). *Kinet. Catal.* **2009**, *50*, 275–283, doi:10.1134/S0023158409020190.

31. Lim, H.S.; Lee, M.; Kim, Y.; Kang, D.; Lee, J.W. Low-temperature CO2 hydrogenation to CO on Ni-incorporated LaCoO3 perovskite catalysts. *Int. J. Hydrogen Energy* **2021**, *46*, 15497–15506, doi:10.1016/j.ijhydene.2021.02.085.

32. Lin, K.H.; Wang, C. Bin; Chien, S.H. Catalytic performance of steam reforming of ethanol at low temperature over LaNiO3 perovskite. *Int. J. Hydrogen Energy*

2013, *38*, 3226–3232, doi:10.1016/j.ijhydene.2013.01.005.

33. Wu, G.; Li, S.; Zhang, C.; Wang, T.; Gong, J. Glycerol steam reforming over perovskite-derived nickel-based catalysts. *Appl. Catal. B Environ.* **2014**, *144*, 277–285, doi:10.1016/j.apcatb.2013.07.028.

34. Nabgan, W.; Tuan Abdullah, T.A.; Mat, R.; Nabgan, B.; Triwahyono, S.; Ripin, A. Hydrogen production from catalytic steam reforming of phenol with bimetallic nickel-cobalt catalyst on various supports. *Appl. Catal. A Gen.* **2016**, *527*, 161–170, doi:10.1016/j.apcata.2016.08.033.

35. González Tejuca, L.; Bell, A.T.; Fierro, J.L.G.; Peña, M.A. Surface behaviour of reduced LaCoO3 as studied by TPD of CO, CO2 and H2 probes and by XPS. *Appl. Surf. Sci.* **1988**, *31*, 301–316, doi:10.1016/0169-4332(88)90095-5.

36. Sunding, M.F.; Hadidi, K.; Diplas, S.; Løvvik, O.M.; Norby, T.E.; Gunnæs, A.E. XPS characterisation of in situ treated lanthanum oxide and hydroxide using tailored charge referencing and peak fitting procedures. *J. Electron Spectros. Relat. Phenomena* **2011**, *184*, 399–409, doi:10.1016/j.elspec.2011.04.002.

37. Ogugua, S.N.; Swart, H.C.; Ntwaeaborwa, O.M. The influence of post-preparation annealing atmospheres on the optical properties and energy transfer between Pr3+ and Dy3+ in mixed lanthanum-yttrium oxyorthosilicate hosts. *Opt. Mater. (Amst).* **2018**, *76*, 125–140, doi:10.1016/j.optmat.2017.12.032.

38. Imada, S.; Jo, T. Effects of hybridization on multiplet structures in 3d- and 4d-core photoemission spectra in light rare earth compounds. *Phys. Scr.* **1990**, *41*, 115–119, doi:10.1088/0031-8949/41/1/028.

39. Islam, M.B.; Yanagida, M.; Shirai, Y.; Nabetani, Y.; Miyano, K. NiO x Hole Transport Layer for Perovskite Solar Cells with Improved Stability and Reproducibility. *ACS Omega* **2017**, *2*, 2291–2299,

doi:10.1021/acsomega.7b00538.

40. Chen, Y.S.; Kang, J.F.; Chen, B.; Gao, B.; Liu, L.F.; Liu, X.Y.; Wang, Y.Y.; Wu, L.; Yu, H.Y.; Wang, J.Y.; et al. Microscopic mechanism for unipolar resistive switching behaviour of nickel oxides. *J. Phys. D. Appl. Phys.* **2012**, *45*, doi:10.1088/0022-3727/45/6/065303.

41. Deka, D.J.; Gunduz, S.; Fitzgerald, T.; Miller, J.T.; Co, A.C.; Ozkan, U.S. Production of syngas with controllable H2/CO ratio by high temperature co-electrolysis of CO2 and H2O over Ni and Co- doped lanthanum strontium ferrite perovskite cathodes. *Appl. Catal. B Environ.* **2019**, *248*, 487–503, doi:10.1016/j.apcatb.2019.02.045.

42. Van Doorn, R.H.E.; Bouwmeester, H.J.M.; Burggraaf, A.J. Kinetic decomposition of La0.3Sr0.7CoO3-δ perovskite membranes during oxygen permeation. *Solid State Ionics* **1998**, *111*, 263–272, doi:10.1016/s0167-2738(98)00191-x.

43. L.C. Pereira, A.; A. dos Santos, N.; L.O. Ferreira, M.; Albornoz, A.; do Carmo Rangel, M. Effect of cobalt on the activity of iron-based catalysts in water gas shift reaction. In; 2007; pp. 225–230.

44. Hwang, K.R.; Lee, C.B.; Park, J.S. Advanced nickel metal catalyst for water-gas shift reaction. *J. Power Sources* **2011**, *196*, 1349–1352, doi:10.1016/j.jpowsour.2010.08.084.

45. Zhang, Z.; Ou, Z.; Qin, C.; Ran, J.; Wu, C. Roles of alkali/alkaline earth metals in steam reforming of biomass tar for hydrogen production over perovskite supported Ni catalysts. *Fuel* **2019**, *257*, 116032, doi:10.1016/j.fuel.2019.116032.

46. Gai, C.; Zhang, F.; Lang, Q.; Liu, T.; Peng, N.; Liu, Z. Facile one-pot synthesis of iron nanoparticles immobilized into the porous hydrochar for catalytic

decomposition of phenol. *Appl. Catal. B Environ.* **2017**, *204*, 566–576, doi:10.1016/j.apcatb.2016.12.005.

47. Wu, G.; Zhang, C.; Li, S.; Han, Z.; Wang, T.; Ma, X.; Gong, J. Hydrogen production via glycerol steam reforming over Ni/Al 2O3: Influence of nickel precursors. *ACS Sustain. Chem. Eng.* **2013**, *1*, 1052–1062, doi:10.1021/sc400123f.

48. Horiuchi, T.; Sakuma, K.; Fukui, T.; Kubo, Y.; Osaki, T.; Mori, T. Suppression of carbon deposition in the CO2-reforming of CH4 by adding basic metal oxides to a Ni/Al2O3 catalyst. *Appl. Catal. A Gen.* **1996**, *144*, 111–120, doi:10.1016/0926-860X(96)00100-7.

49. Zhuang, Q.; Qin*, Y.; Chang, L. Promoting effect of cerium oxide in supported nickel catalyst for hydrocarbon steam-reforming. *Appl. Catal.* **1991**, *70*, 1–8, doi:10.1016/S0166-9834(00)84149-4.

50. Adnan, M.A.; Muraza, O.; Razzak, S.A.; Hossain, M.M.; De Lasa, H.I. Iron Oxide over Silica-Doped Alumina Catalyst for Catalytic Steam Reforming of Toluene as a Surrogate Tar Biomass Species. *Energy and Fuels* **2017**, *31*, 7471–7481, doi:10.1021/acs.energyfuels.7b01301.

51. Łamacz, A.; Babiński, P.; Łabojko, G. The impact of components of synthesis gas from coal gasification on conversion of model tar compounds over Ni/CeZrO2 catalyst. *Fuel* **2019**, *236*, 984–992, doi:10.1016/j.fuel.2018.09.075.